PAPER • OPEN ACCESS

Model for second harmonic ECRH plasma start-up in stellarators

OPEN ACCESS
IOP Publishing | International Atomic Energy Agency
Nuclear Fusion
Nucl. Fusion **66** (2026) 026011 (13pp)
https://doi.org/10.1088/1741-4326/ae2b84

Model for second harmonic ECRH plasma start-up in stellarators

C. Albert Johansson[1,*], **Pavel Aleynikov**[1], **Alvaro Cappa**[2] **and the W7-X Team**[a]

[1] Max Planck Institute for Plasma Physics, Wendelsteinstraße 1, 17491 Greifswald, Germany
[2] Laboratorio Nacional de Fusión, CIEMAT, 28040 Madrid, Spain

E-mail: albert.johansson@ipp.mpg.de

Received 31 July 2025, revised 15 November 2025
Accepted for publication 11 December 2025
Published 29 December 2025

Abstract

Plasma ionisation avalanche under constant electric field is well described by classical theory. It is the standard tokamak start-up method. In this work, we investigate an analogous avalanche process driven by electron cyclotron resonance (ECR). This is a typical plasma initiation method in stellarators. At low plasma temperatures, the typical wave–particle interactions result in complex trajectories. These allow electrons to gain energy beyond their initial value in a single wave encounter. We present a heating model applicable to the standard second-harmonic start-up in stellarators. The model is based on scaling laws derived from wave–particle Hamiltonian dynamics. It relies on a dimensionless numerical coefficient that encapsulates geometric and experimental specifics. This coefficient is calibrated via test-particle simulations. The absorption model is coupled with a collisional-radiative description of hydrogen ionisation, radiation losses, and recombination to simulate the evolution of the ECR-driven ionisation avalanche. The breakdown condition is shown to be related to the maximum temperature achieved during the early stages of start-up. A semi-analytical expression for this temperature is given. The predicted plasma breakdown times show reasonable agreement with experimental observations in the Wendelstein 7-X and TJ-II stellarators.

Keywords: ECRH, breakdown, start-up, ionisation avalanche, W7-X, TJ-II, stellarator

(Some figures may appear in colour only in the online journal)

1. Introduction

Plasma initiation can be achieved through various heating mechanisms. In present stellarators, electron cyclotron resonance heating (ECRH) is the typical method for energising electrons. These energised electrons collide with neutrals, leading to ionisation and triggering an avalanche process that results in plasma formation.

In contrast, present-day tokamaks initiate the avalanche primarily through an inductive electric field. The initial phase of this global electric field is called Townsend avalanche [1]. This is followed by the burn-through phase and a current ramp. The resulting electron population generates a toroidal plasma current, which ultimately defines the equilibrium magnetic configuration (for a comprehensive overview of tokamak start-up, see, e.g. Mueller [2]). The Paschen curve [3] has been identified as the criterion for an inductive ionisation avalanche in tokamaks.

Restrictions imposed on the maximum achievable inductive field strength can benefit from the use of an ECRH assisted start-up, thereby reducing the minimum loop voltage required. This reduction is especially important in

[a] See Grulke *et al* 2024 (https://doi.org/10.1088/1741-4326/ad2f4d) for the W7-X Team.
[*] Author to whom any correspondence should be addressed.

large superconducting tokamaks, such as ITER [4]. The fundamental and second harmonic ECRH-assisted start-up has been investigated in devices such as DIII-D [5, 6], Tora Supre [7], AUG [8], FTU [9], KSTAR [10], or JT-60U [11], demonstrating that its use ensures reliable and reproducible plasma discharges over a broader operational range.

Even though stellarators routinely utilise ECRH for plasma formation, the condition for ECRH-driven ionisation avalanches in stellarators has yet to be determined. This is despite it having several advantages over the tokamak start-up, such as initialising the magnetic configuration before the plasma generation. Therefore, the ECRH-assisted start-up in tokamaks, which involves additional important physical phenomena (flux surface formation, loop voltage, *etc*), will not be addressed here. Instead, the primary objective of this work is to establish the breakdown criteria for ECRH-driven start-up in a stellarator.

In order to model ECRH-driven ionisation avalanches, it is first necessary to develop a comprehensive understanding of resonant power absorption at the very early stages of plasma formation. In this study, we characterise electron cyclotron resonance (ECR) power absorption for the second-harmonic X-mode waves, which are employed to initiate breakdown in Wendelstein 7-X. The absorption model is coupled to a hydrogen gas model to describe the evolution of the ionisation avalanche. A condition for the power threshold required to achieve breakdown is deduced.

The seminal work of Cappa and Castejón [12] utilised an effective ECR interaction width [13] to determine the electron distribution function. Moreover, in the model described in Cappa and Castejón [12], the simplified non-linear energy source developed in [13] was implemented using an average stray radiation intensity homogeneously distributed around the torus with half of its polarisation in the right hand mode. The direct interaction with localised beam power, which does not meet the conditions for magnetic field structure assumed in [13], was disregarded. In addition, this effective interaction falls short in capturing key dependencies that have been observed in experimental contexts (see Cappa *et al* [14]). In particular, the influence of the parallel refractive index, beam width [15] and magnetic field inhomogeneity [16] on the breakdown condition is not accounted for.

Capturing these dependencies can be achieved through analysis of the Hamiltonian dynamics of the wave–particle interaction. The relevant Hamiltonian formalism [17–19] has been studied in detail in the adiabatic regime, wherein it is assumed that a particle undergoes an extended interaction with the beam prior to decorrelation (e.g. in [15, 18–23]). In contrast, interaction with fast decorrelation is described by the quasi-linear regime (e.g. in [24–27]). However, the plasma conditions during the ionisation avalanche in a stellarator typically fall outside both these regimes. Nevertheless, the Hamiltonian approach provides insight into how energy absorption scales with key physical parameters. The absorption can thus be reduced to a general scaling law multiplied by a functional that depends on magnetic geometry, ECRH beam configuration, and the electron distribution function. This functional is studied numerically for Maxwell distributed electrons, and is found to attain values of 25-800, where the most important parameters are the magnetic field structure and beam width.

The absorption model, when paired with the ionisation, recombination and radiation processes in a 1D cylindrical diffusive model, is capable of characterising the ionisation-avalanche stage.

The work is organised in the following way. Initially, the beam absorption is considered. Secondly, the neutral-ion model is presented. Thirdly, the model is compared to experimental data from W7-X, wherein the model predicts a stage with a quasi-steady state temperature. Finally, a relation between power and achieved steady-state temperature is derived. Time to achieve breakdown is compared to previous TJII discharges.

2. Model for second harmonic ECRH absorption

The power absorption is characterised by the attenuation coefficient. It is given by the negative power absorbed by the electrons averaged over velocity space and integrated over the surface orthogonal to the wave vector, divided by the power:

$$\frac{1}{P}\frac{\partial P}{\partial z} = -\frac{1}{P}\iint n_e \langle mc^2 \frac{\mathrm{d}\gamma}{\mathrm{d}t}\rangle_v \,\mathrm{d}x\,\mathrm{d}y, \tag{1}$$

where n_e is the electron density, γ is the electron relativistic Lorentz factor, and the average $\langle\cdot\rangle_v = \iiint \cdot f \mathrm{d}^3 v$ is the velocity space average, where the distribution function $f(r, v, t)$ is normalised to unity such that $\langle 1\rangle_v = 1$.

For the sake of convenience the power absorption length scale is defined in this work through a direction that is orthogonal to the magnetic field. We therefore choose the coordinates to be defined such that $\hat{x}$ is aligned with the magnetic-field direction and $\hat{z} \parallel \hat{x} \times (\boldsymbol{k} \times \hat{x})$ where $\boldsymbol{k}$ is the wave vector, and call it *the modified attenuation coefficient*. Due to the fact that the wave extent is typically negligible in comparison to the machine size, the bending of the magnetic field lines is ignored.

The time derivative of the energy can be expressed as $\frac{\mathrm{d}\gamma}{\mathrm{d}t} = \frac{\mathrm{d}\gamma}{\mathrm{d}x} v_x$. In accordance with the principle of phase space conservation, the function $f n_e v_x$ remains constant. Consequently, the integration over x can be carried out analytically, thereby yielding the energy gain per single beam crossing, $\Delta\gamma$. In the integration leading to $\Delta\gamma$, the change of variables from time to space, $t \mapsto x$ introduces a sign reversal for negative velocities, resulting in $v_x \mapsto |v_x|$. The ionisation and recombination that occur inside the small wave-field extent is ignored.

The quantity $\langle \Delta\gamma |v_x| \rangle_v$ determines the modified attenuation coefficient. The interaction between the wave and electrons is

governed by a Hamiltonian. The Hamiltonian for second harmonic interaction is given by

$$H = mc^2\sqrt{1+\frac{2eBI}{m^2c^2}+\frac{\left(\frac{k_\parallel}{2}I+P_x\right)^2}{m^2c^2}}-\frac{\omega}{2}I + \frac{N_\perp E}{2cB}\frac{\omega}{2}I\cos(2\chi), \tag{2}$$

where $I=\frac{p_\perp^2}{2eB}$ is the magnetic moment times m/e, and conjugates to the gyro-phase variable $\chi=\zeta-\frac{\omega}{2}t+\frac{1}{2}\boldsymbol{k}\cdot\boldsymbol{R}$, where ζ is a gyro-angle, ω the wave-frequency, and $\boldsymbol{R}$ the guiding-centre position. The wave-vector is denoted by $\boldsymbol{k}$, and $k_\parallel$ and $k_\perp$ refer to the magnitude of the parallel and perpendicular components of $\boldsymbol{k}$ with respect to the magnetic field $\boldsymbol{B}$. The canonical momentum $P_x=p_\parallel-\frac{k_\parallel}{2}I$ is conjugate to the coordinate x. B denotes the magnetic field strength, e the elementary charge, m the electron mass, c the speed of light and $N_\perp=k_\perp\omega/c$. Here, E is the electric field strength, assuming linear polarisation. For arbitrary polarisation, E should be replaced by twice the part of the electric field rotating in the electron direction, orthogonal to the magnetic field. See f.e. [28, 29] and references therein. For $k_\parallel\approx 0$, this corresponds to the X2-mode polarisation.

Since the Hamiltonian is explicitly time-independent, the electron phase space trajectory and therefore its energy gain are fully determined by the initial conditions. Representative orbits are demonstrated in figure 1. Electrons with high parallel velocity experience a small energy kick. An example of such trajectory is provided in the left panel of figure 1. When multiple such kicks determines the heating rate, quasi-linear theory applies (see e.g. [24, 25, 27, 30]). In contrast in the adiabatic regime (right panel) the electron experiences multiple energy excursion as it traverses the beam. Consequently, its motion can be characterised by an additional adiabatic invariant, whereby the energy change becomes known (see e.g. [15, 17, 19, 22]).

However, during the initial stages of ionisation avalanche, neither of these limiting regimes is expected to apply. Instead, electrons may experience energy jumps significantly larger than their typical energy, yet without a clear time-scale separation that would permit a simplification. Examples of such trajectories are demonstrated in the central panel of figure 1. Whilst it is only possible to obtain $\Delta\gamma$ numerically within this regime, the structure of the Hamiltonian equation (2) will be exploited in order to extract the key scaling dependencies of the energy gain.

Unless the electron is in the adiabatic regime, only even powers of the E term contribute to the average energy gain, due to the phase-averaging over the initial value of χ. Since E is a small parameter, we expect the energy gain to scale as E^2. Indeed, in the small kick regime, an analytical expression for the change in the action ΔI can be obtained. Averaging over

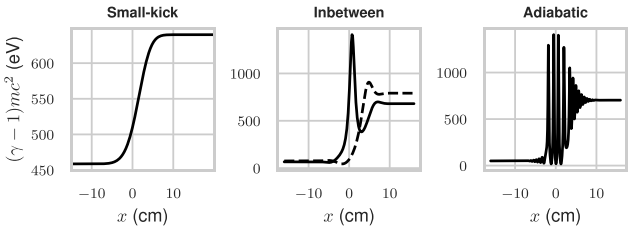

Figure 1. Example electron orbits from equation (2) for different initial parallel velocity. Wave frequency is 140 GHz, with 800 kW spread over a 4 cm beam waist Gaussian beam. The wave polarisation is linear and the electric field is perpendicular to the background magnetic field. Magnetic field strength is constant $B=2.502\,548$ T and orthogonal to the wave vector.

the initial phase χ yields:

$$\frac{1}{I}\int_0^{2\pi}\Delta I\mathrm{d}\chi\approx\frac{\pi}{2}\left(\int\frac{N_\perp E}{cB}\frac{\omega}{2}\mathrm{d}t\right)^2\sim\frac{\pi}{2}\frac{N_\perp^2E^2}{c^2B^2}\frac{\omega^2}{4}\Delta t^2. \tag{3}$$

Using $\langle\Delta\gamma|v_x|\rangle_v\propto E^2$ leaves an unknown proportionality function A:

$$\frac{\langle\Delta\gamma|v_x|\rangle_v}{\langle|v_x|\rangle_v}=A\frac{N_\perp^2}{c^2B^2}\frac{4\eta P}{\pi w^2}, \tag{4}$$

where $A\equiv A(\frac{k_\parallel c}{\omega},\frac{w\omega}{c},\frac{\omega I}{mc^2},\frac{P_x}{mc})[\frac{eB}{m\omega}]$ depends on the independent parameters of the Hamiltonian, and is determined by the exact wave–particle interaction. These parameters are the parallel wave-vector $k_\parallel$, beam width w, initial value of the velocity-space coordinates and it is a functional of the magnetic-field strength $B(z)$ [16]. The wave frequency ω determines the time-scale normalisation. Normalisation is such that A is dimensionless, where E is related to the power through $P=\frac{\pi w^2}{2}\frac{E^2}{2\eta}$, where η is the vacuum impedance.

That $\langle\Delta\gamma|v_x|\rangle_v\propto E^2$ implies that the modified attenuation coefficient is independent of wave power, or $\langle\Delta\gamma|v_x|\rangle_v\rangle_v\propto P\times p_{\mathrm{profile}}$, where p_{profile} is the local wave intensity profile. The modified attenuation coefficient can be expressed as

$$\frac{1}{P}\frac{\partial P}{\partial z}=-\langle n_e\rangle_y\frac{mc^2\langle\Delta\gamma|v_x|\rangle_{v,\max}}{P}F, \tag{5}$$

where $\langle\Delta\gamma|v_x|\rangle_{v,\max}$ is the velocity-space average of the product of energy gain and initial particle velocity, evaluated along the path that intersects the peak electric field. The transverse density weighting is defined by:

$$\langle n_e\rangle_y\equiv\frac{\int n_e p_{\mathrm{profile}}\,\mathrm{d}y}{F}, \tag{6}$$

where $F(z)\equiv\int p_{\mathrm{profile}}\mathrm{d}y$ is the power form factor. For a Gaussian beam, the form factor reduced to $F=\sqrt{\pi/2}w(z)$, where $w(z)$ denotes the beam waist. We denote the value of A at maximum field along y with $\bar{A}$. The modified attenuation coefficient is

$$\frac{1}{P}\frac{\partial P}{\partial z}=-F\langle\bar{A}n_e\rangle_y m\frac{N_\perp^2}{B^2}\frac{4\eta}{\pi w^2}\langle|v_x|\rangle_v. \tag{7}$$

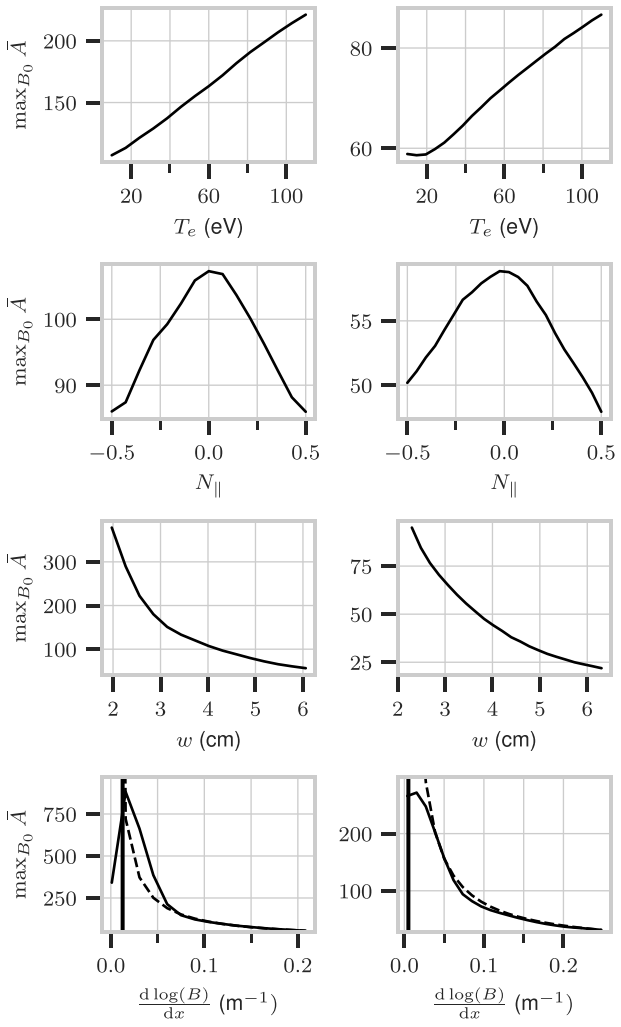

Figure 2. The coefficient $\bar{A}$ dependences on different parameters variations in solid lines. In the left-hand column, non-varying parameters are held fixed at reference values: $N_\parallel = 0, P = 0.5\,\mathrm{MW}, w = 4\,\mathrm{cm}$, $\frac{\mathrm{d}\ln B}{\mathrm{d}z} = 0.1\,\mathrm{m}^{-1}, T = 10\,\mathrm{eV}$ and $\omega/2\pi = 140.2\,\mathrm{GHz}$. In the right-hand column, these values are: $N_\parallel = 0, P = 0.2\,\mathrm{MW}, w = 3.3\,\mathrm{cm}$, $\frac{\mathrm{d}\ln B}{\mathrm{d}z} = 0.13\,\mathrm{m}^{-1}, T = 10\,\mathrm{eV}$ and $\omega/2\pi = 53.2\,\mathrm{GHz}$. The expected $1/\frac{\mathrm{d}\ln B}{\mathrm{d}x}$ dependence for large $1/\frac{\mathrm{d}\ln B}{\mathrm{d}x}$ dependence is shown with a dashed line, where the critical gradient for this scaling is marked with a vertical line. To obtain A for a different wave frequency, lengths must be normalised to c/ω (see the arguments for A given after equation (4)).

To evaluate the parameter $\bar{A}$, we numerically solve the equations of motion (equation (3.7) in [16]), and use the resulting trajectories to compute the absorption via equation (5). The corresponding value of $\bar{A}$ is then extracted from equation (7).

Figure 2 illustrates the parametric dependence of the averaged coefficient $\bar{A}$. The parameters were varied over the following ranges: $N_\parallel \in [-0.5, 0.5]$, $w \in [2\,\mathrm{cm}, 6\,\mathrm{cm}]$, and $T_e \in [10\,\mathrm{eV}, 110\,\mathrm{eV}]$. The B-field derivative ranges from $\frac{\mathrm{d}\ln B}{\mathrm{d}z} \in [0.016\,\mathrm{m}^{-1}, 0.19\,\mathrm{m}^{-1}]$ in the left-hand column, and $\frac{\mathrm{d}\ln B}{\mathrm{d}z} \in [0.004\,\mathrm{m}^{-1}, 0.24\,\mathrm{m}^{-1}]$ in the right-hand column.

When varying one parameter, each of the others attain their own reference value. The two columns share the reference values $N_\parallel = 0$, and $T = 10\,\mathrm{eV}$. The reference values for the input power P, beam width w, and magnetic field gradient $\frac{\mathrm{d}\ln B}{\mathrm{d}z}$, are slightly different in the two columns. In the left-hand column, these values are chosen to be similar to those of W7-X, while those in the right-hand column are similar to those of TJ-II. In the left-hand column, $P = 0.5\,\mathrm{MW}$, $w = 4\,\mathrm{cm}$, and $\frac{\mathrm{d}\ln B}{\mathrm{d}z} = 0.1\,\mathrm{m}^{-1}$, whereas in the right-hand column $P = 0.2\,\mathrm{MW}, w = 3.3\,\mathrm{cm}$, and $\frac{\mathrm{d}\ln B}{\mathrm{d}z} = 0.13\,\mathrm{m}^{-1}$. In the left-hand column, the wave-frequency corresponds to that used in W7-X: $\omega/2\pi = 140.2\,\mathrm{GHz}$, whereas in the right-hand column it corresponds to that utilised in TJ-II: $\omega/2\pi = 53.2\,\mathrm{GHz}$.

The magnetic field strength on the beam axis, B_0, is selected to maximise $\bar{A}$. This is justified by the observation that the beam traverses a range of magnetic field strengths and will typically encounter the optimal value along its path.

Below, we analyse the dependencies obtained from rigorous trajectory calculations and provide corresponding estimates where appropriate limits exist.

For most parameters $\bar{A}$ is close to 100. The temperature scaling does not follow the quasi-linear scaling, which would prohibit absorption near $T_e = 0$. The difference between the left-hand and right-hand column of figure 2 can be explained by noting that $\bar{A}$ is almost proportional to $\omega \approx 2eB/m$ if the rest of the parameters are kept constant in SI-units. This is realised by inspecting equation (7), where one power of B normalises v_x, which has a minor impact on the value of $\bar{A}$, leaving only one power of B, i.e. one power of ω.

The most significant parameter that enhances the resonance is the magnetic field derivative along the field line. Johansson and Aleynikov [16] demonstrated that a magnetic field derivative can yield a strong correlated interaction and enhancement to the energy gain, that is $\bar{A}$ reaches high values. However, at fixed derivative, $\bar{A}$ can often be treated as constant.

In the limit of strong magnetic field gradient along the field line, the energy gain observed in figure 1 is limited by detuning in the resonance parameter χ. Accordingly, optimal interaction occurs when the change of χ is of order unity.

Assuming that $\frac{\mathrm{d}\ln(B)}{\mathrm{d}x}$ sets the characteristic detuning timescale, the corresponding interaction time can be estimated as

$$\Delta t \sim \sqrt{\frac{2m^2}{eB_0 \frac{\mathrm{d}\ln(B)}{\mathrm{d}x} p_\parallel}}, \tag{8}$$

where the $p_\parallel$ is assumed to be constant within the beam. Substituting this into the expression for the interaction strength, equation (3), one finds that the average amplitude $\bar{A}$ scales as $1/\frac{\mathrm{d}\ln(B)}{\mathrm{d}x}$ in the high-gradient limit. This scaling is indeed observed numerically as shown in the fourth panel of figure 2. The anticipated $1/\frac{\mathrm{d}\ln(B)}{\mathrm{d}x}$ scaling is indicated by the dashed lines and agrees well with the numerical results for sufficiently large $\frac{\mathrm{d}\ln(B)}{\mathrm{d}x}$.

However, the scaling changes if the intrinsic frequency of the nonlinear energy excursion, the energy oscillations in right

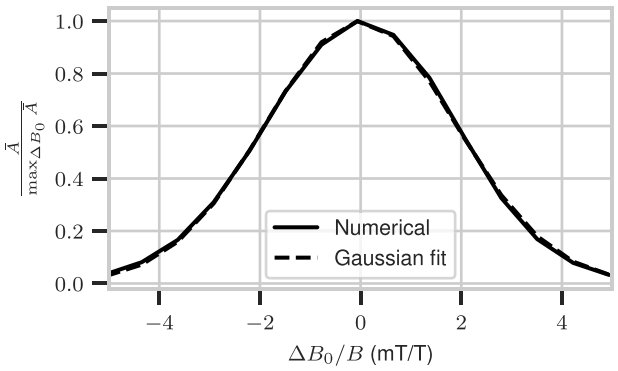

Figure 3. Gaussian fit of the absorption amplitude $\bar{A}$ as a function of ΔB_0, using the reference parameters from figure 2.

panel of figure 1, exceeds the detuning frequency imposed by $\frac{\mathrm{d}\ln(B)}{\mathrm{d}x}$. In such cases, the gradient is irrelevant for detuning. The nonlinear excursion frequency in our case is approximately (see also Seol *et al* [15]),

$$f_{\mathrm{nl}} = E \times 93.3\,\mathrm{Hz\,m\,V^{-1}}. \tag{9}$$

Equating this frequency to the detuning rate yields a critical gradient, beyond which nonlinear dynamics dominate:

$$\left.\frac{\mathrm{d}\ln(B)}{\mathrm{d}x}\right|_{\mathrm{crit}} = \frac{4\sqrt{2}m^{3/2}\left(E \times 93.3\,\mathrm{Hz\,m\,V^{-1}}\right)^2}{eB_0\sqrt{T}}. \tag{10}$$

The critical gradient given in equation (10) is indicated with the vertical lines.

The parameters discussed above, namely T_e, $N_\parallel$, w and $\frac{\mathrm{d}\ln B}{\mathrm{d}x}$, govern the integrated power absorption length scale for the optimal B_0. The width of the absorption profile is governed by the dependence of $\bar{A}$ on the magnetic field strength B_0, with $\Delta B_0 = 0$ corresponding to the optimal interaction condition. In the small kick regime, the absorption amplitude is proportional to E^2, evaluated in the vicinity of this optimal B_0. At a different field line, the location of optimal B is shifted along the magnetic field line by δx such that $\Delta B_0/B = \frac{\mathrm{d}\ln(B)}{\mathrm{d}x}\,\delta x$. At this location, the value of E^2 is modulated by its Gaussian transverse profile, yielding a factor

$$\exp\left(-\frac{2\delta x^2\left(1-N_\parallel^2\right)}{w^2}\right) = \exp\left(-\frac{2\Delta B_0^2\left(1-N_\parallel^2\right)}{B^2\left(\frac{\mathrm{d}\ln(B)}{\mathrm{d}x}\right)^2 w^2}\right).$$

Accordingly, the absorption profile is expected to exhibit a Gaussian dependence on ΔB_0:

$$\bar{A} = \max_{B_0}(\bar{A}) \cdot \exp\left(-\frac{(\Delta B_0/B)^2}{d^2}\right), \tag{11}$$

where a fit of this form to the numerical results using reference parameters is shown in figure 3.

The dependence of the Gaussian width parameter d on system parameters is shown in figure 4, over the same parameter

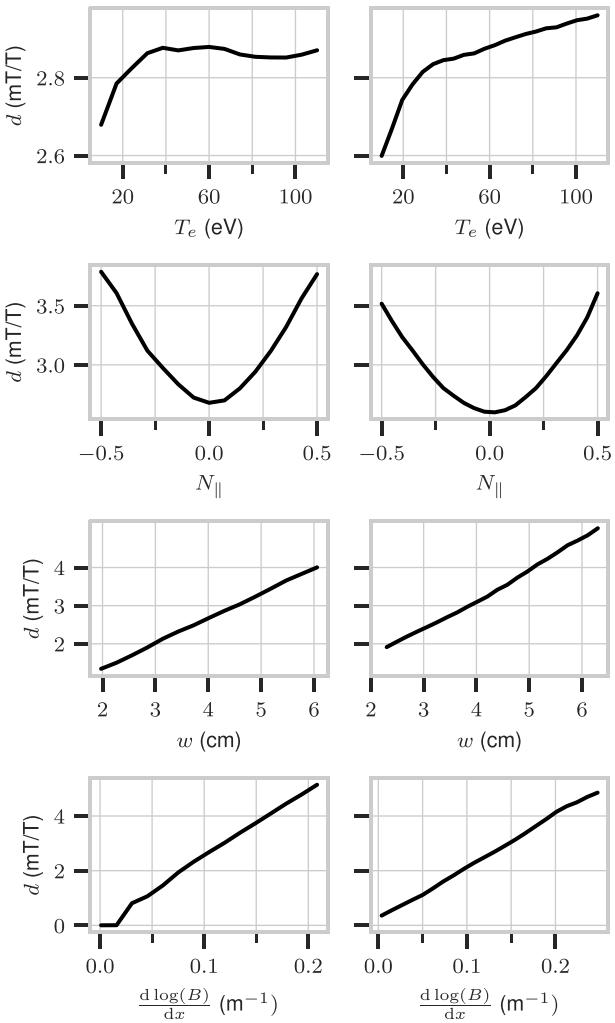

Figure 4. Variation of the Gaussian width parameter d across the same parameter space as shown in figure 2.

space as $\max_{B_0}\bar{A}$ in figure 2. As anticipated, d scales linearly with both $\frac{\mathrm{d}\ln(B)}{\mathrm{d}x}$ and the beam width w.

The spatial extent of the absorption region across the field line can therefore be approximated as a Gaussian with characteristic length scale $L = d/\frac{\mathrm{d}\ln(B)}{\mathrm{d}z}$, by identifying $\Delta B_0 \approx \frac{\mathrm{d}\ln(B)}{\mathrm{d}z}z$.

Finally, we verify the power scaling assumption introduced in equation equation (4). The power dependence of $\bar{A}$ is shown in figure 5. As expected, the $\bar{A}$ becomes independent of wave power for higher temperatures (i.e. within the small kick regime). In the low-temperature regime relevant to our study, $\bar{A}$ exhibits a power dependence due to the nonlinear nature of wave–particle interactions. However, within the parameter range of interest, this variation remains within 30%, and is therefore neglected in our analysis of plasma start-up.

In summary, equation (7) provides the absorption for electrons crossing the beam once (fast-traversing, adiabatic or anything in between), where the function $\bar{A}$ has been studied numerically. In the following sections, equation (7) will determine the absorbed power, and $\bar{A}$ is approximated using the data shown in figure 2.

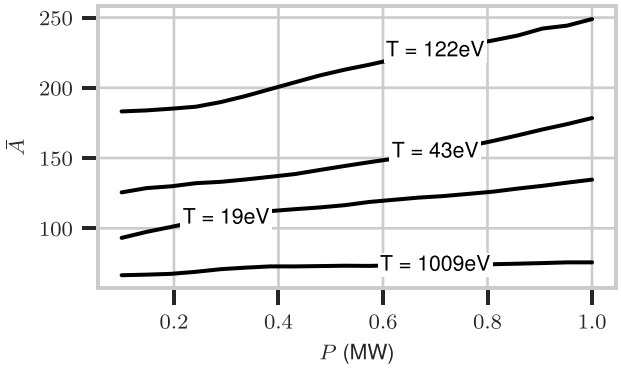

Figure 5. $\bar{A}$ dependency on power.

3. Ionisation-avalanche model

The ionisation process is predominantly driven by the thermal bulk as long as the neutral density is sufficiently high. This occurs despite of the acceleration of a supra-thermal population driven by the wave–particle interaction [31]. The bulk primarily drives ionisation due to two factors: Firstly, the ionisation rate coefficient exhibits a maximum at approximately 100 eV and remains high at lower energies. Secondly, during the initial phase of the ionisation avalanche process, the thermal bulk experiences an exponential increase in density. Furthermore, because of the low density of supra-thermal electrons, their contribution to the energy balance is negligible. Consequently, the influence of the wave is considered to be the indirect heating of the thermal bulk plasma, as outlined in the preceding section's power absorption model.

The atomic and molecular processes under consideration are

$$\mathrm{H} + \mathrm{e} \longrightarrow \mathrm{H}^+ + 2\mathrm{e} \tag{12}$$
$$\mathrm{H}_2^+ + \mathrm{H} \longrightarrow \mathrm{H}^+ + \mathrm{H}_2 \tag{13}$$
$$\mathrm{e} + \mathrm{H}_2 \longrightarrow \mathrm{e} + 2\mathrm{H} \tag{14}$$
$$\mathrm{e} + \mathrm{H}_2 \longrightarrow 2\mathrm{e} + \mathrm{H}_2^+ \tag{15}$$
$$\mathrm{H}^+ + \mathrm{H}_2 \longrightarrow \mathrm{H} + \mathrm{H}_2^+ \tag{16}$$
$$\mathrm{e} + \mathrm{H}^+ \longrightarrow \mathrm{H} \tag{17}$$
$$\mathrm{e} + \mathrm{H}_2^+ \longrightarrow 2\mathrm{H} \tag{18}$$
$$\mathrm{e} + \mathrm{H}_2^+ \longrightarrow \mathrm{e} + \mathrm{H} + \mathrm{H}^+ \tag{19}$$
$$\mathrm{H}_2 + \mathrm{H}_2^+ \longrightarrow \mathrm{H}_2^+ + \mathrm{H}_2 \tag{20}$$
$$\mathrm{H} + \mathrm{H}^+ \longrightarrow \mathrm{H}^+ + \mathrm{H}. \tag{21}$$

The rate coefficients are calculated using EIRENE fits [32], except for the ionisation of H and the recombination of H^+, for which data are taken from the ADAS database [33]. The coefficients equations (13), (16), (20) and (21) are calculated as Hollmann *et al* [34]. The ADAS rate coefficient assumes an equation for each (meta)stable excited atom. Hydrogen has two such states: 1 s and 2 s. However, we combine these into one because the neutral density quickly becomes isotropic across the entire machine.

The density of the neutral species evolves according to

$$\frac{\partial n_n}{\partial t} = \frac{1}{r}\frac{\partial}{\partial r}\left(rD_n\frac{\partial n_n}{\partial r}\right) + \sum_j n_{1,j}n_{2,j}R_j\sigma_{i,j}, \tag{22}$$

where $\sigma_{i,j}$ are the stoichiometric coefficients for element i of reaction j, R_j is the rate coefficient for the process j, $n_{1,j}$ and $n_{2,j}$ are the densities of the reactants. The sum is taken over all reactions (equations (12)–(21)). The neutral diffusion coefficient D_n is calculated as [34]

$$D_n = \frac{D_{\mathrm{th}}}{1 + \frac{D_{\mathrm{th}}\nabla n}{\frac{1}{4}n_n v_{\mathrm{th}}}}, \tag{23}$$

where $D_{\mathrm{th}} = v_{\mathrm{th}}^2/\nu_n$ is an approximate thermal diffusion coefficient, $v_{\mathrm{th}} = \sqrt{kT_n/m_n}$ is the thermal speed with $T_n = 300\,\mathrm{K}$, and ν_n is the total collision frequency (see Hollmann *et al* [34] near equation (A.2) for details). This form ensures that the neutral flux does not exceed a quarter of the thermal speed, which is consistent with kinetic theory. In essence, this diffusion is extremely rapid, and distributes the neutrals evenly and quickly across all radii.

The ion densities are modelled analogously to the neutral species:

$$\frac{\partial n_i}{\partial t} = \frac{1}{r}\frac{\partial}{\partial r}\left(rL_{11}\frac{\partial n_i}{\partial r}\right) + \sum_j n_{1,j}n_{2,j}R_j\sigma_j, \tag{24}$$

where L_{11} is the Maxwell-averaged diffusion-coefficient (see e.g. Beidler *et al* [35]). This coefficient is computed by approximating the mono-energetic collision-frequency with its Maxwellian average. This enables pre-computation of L_{11} for a significant numerical speed-up at the expense of accuracy. Unlike neutrals, ion diffusion occurs on timescales much longer than the ionisation avalanche and therefore plays a secondary role in the avalanche dynamics. The electron density is calculated using the condition for quasi-neutrality.

The electron temperature and the ion temperature are assumed to be equal and are calculated using energy balance,

$$\begin{aligned}\frac{\partial}{\partial t}\left[\left(\frac{3}{2}n_e + \frac{3}{2}n_{\mathrm{H}^+} + \frac{7}{2}n_{\mathrm{H}_2^+}\right)T_e\right] &= p_{\mathrm{abs}} - p_{\mathrm{loss}} \\ &+ \frac{\left(\frac{3}{2}n_e + \frac{3}{2}n_{\mathrm{H}^+} + \frac{7}{2}n_{\mathrm{H}_2^+}\right)}{r}\frac{\partial}{\partial r}\left(rL_{22}\frac{\partial T_e}{\partial r}\right),\end{aligned} \tag{25}$$

where p_{abs} and p_{loss} represent the absorbed and lost power per volume, respectively. The diffusion term is the Maxwell-averaged neoclassical electron diffusion coefficient L_{22} [35]. As we will see later, the transport does not greatly affect the core temperature value, which is mainly determined by power balance. L_{22} is computed analogously to L_{11}. Here, H_2^+ is assumed to have seven degrees of freedom: three translational, two vibrational and two rotational. These internal modes are saturated for H_2 at temperatures exceeding 0.6 eV [36]. The temperature equation can be reformulated to

$$\frac{\partial T_e}{\partial t} = \frac{1}{r}\frac{\partial}{\partial r}\left(rL_{22}\frac{\partial T_e}{\partial r}\right) + \hat{S} - \hat{L}. \tag{26}$$

A normalised source term was defined as

$$\hat{S} = \frac{2p_{\text{abs}}}{\bar{d}n_e}, \tag{27}$$

and a normalised loss through

$$\hat{L} \equiv \frac{2p_{\text{loss}}}{\bar{d}n_e} - \frac{2T_e}{\bar{d}n_e}\left(\frac{\partial \frac{3}{2}n_e + \frac{3}{2}n_{\text{H}^+} + \frac{7}{2}n_{\text{H}_2^+}}{\partial t}\right). \tag{28}$$

The averaged degrees of freedom $\bar{d}$ is given by

$$\bar{d} \equiv 3 + 3\frac{n_{\text{H}^+}}{n_e} + 7\frac{n_{\text{H}_2^+}}{n_e}. \tag{29}$$

The power loss is divided into several components:

$$p_{\text{loss}} = p_{\text{rad}} + p_{\text{i}} + p_{\text{d}} + p_{\text{CX}} + p_{\text{R}}, \tag{30}$$

where p_{rad} represents radiation, p_{i} represents the ionisation losses, p_{d} represents dissociation loss, p_{CX} represents the losses associated with charge exchange between a neutral and a charged particle, and finally p_{R} represents the loss due to recombination.

The radiation loss takes both continuum power and line power into account:

$$\begin{aligned} p_{\text{rad}} = {} & R_{\text{line}} n_e \left(n_H + 2n_{\text{H}_2} + n_{\text{H}_2^+}\right) \\ & + R_{\text{cont}} n_e \left(n_{\text{H}^+} + n_{\text{H}_2^+}\right). \end{aligned} \tag{31}$$

The rate coefficients for line power R_{line} and continuum power R_{cont} are calculated using the ADAS database [33]. Accordingly, the corresponding loss terms are evaluated using the total density of H, and H^+. The line radiation is the dominant loss mechanism during a successful breakdown.

The ionisation loss is given by

$$p_{\text{i}} = 13.6\,\text{eV}\max\left(0, \left(\frac{\partial n_e}{\partial t}\right)_{\text{coll.}}\right), \tag{32}$$

where the partial derivative is taken with respect to all ionisation and recombination processes. Each time an electron is created, 13.6 eV is lost from the internal energy due to the ionisation potential. Balance of recombination and ionisation does not impact the collisional derivative of the electron density, $\left(\frac{\partial n_e}{\partial t}\right)_{\text{coll.}}$, but this energy loss is accounted for in the continuum radiation loss term.

The dissociation loss is given by

$$p_{\text{d}} = n_e n_{\text{H}_2} R_{\text{equation(14)}} 10.5\,\text{eV} + n_e n_{\text{H}_2^+} R_{\text{equation(19)}} 6.2\,\text{eV}, \tag{33}$$

where the energy change is taken as the average energy change of charged particles as listed by Janev *et al* [37].

Charge exchange losses are modelled on the basis of an immediate energy loss to the wall by the charge exchange neutral, thanks to its very long mean free path. This is equivalent to assuming that previous ion energy is lost to the wall, i.e.

$$p_{\text{CX}} = \sum_j \frac{d_j}{2} T_e R_{\text{CX},j} n_{1,j} n_{2,j}, \tag{34}$$

where d_j is the degree of freedom of the ion. The sum is taken over the charge exchange processes equations (13, (16), (20) and (21). This loss term is dominant in a very slow or failed breakdown.

Similarly to the charge exchange, the recombination loss accounts for the loss of previous ion energy to the wall

$$p_{\text{R}} = R_{\text{equation(19)}} n_e n_{\text{H}_2^+} \frac{7}{4} T_e + \sum_j \left(\frac{3}{2} + \frac{d_j}{2}\right) T_e n_e n_j R_j, \tag{35}$$

where the sum is taken over recombination events equations (17) and (18). We assumed that H attain half the energy of H_2^+ in equation (19) (and is thus lost).

The heating p_{abs} is determined by the absorbed power through equation (7), which is spread over the full cylindrical volume:

$$p_{\text{abs}} = -\frac{\partial^3 P}{\partial x \partial y \partial z} = -\frac{\text{d}P}{\text{d}r}\frac{1}{4\pi^2 r R_0}, \tag{36}$$

where R_0 is the (effective) major radius. In an off-axis heating scenario, where the electron orbits that pass through the ECRH beam cover the entire flux surface (for example, irrational iota), the surface area $4\pi^2 r R_0$ is to be replaced with $\frac{\partial V}{\partial r}$. Here V denotes the flux surface volume. When (collisional) electron orbits that pass through the ECRH beam do not cover the entire flux surface, a 1D radial model is inaccurate.

When on-axis heating is utilised, the radial deposition-profile is obtained by accounting for the Gaussian beam profile $p_{\text{profile}} = \exp(-2y^2/w^2)$ and a Gaussian profile in z direction. According to equation (11), this has a width of $L = \frac{d}{\frac{\text{d}\ln B}{\text{d}z}}$. Assuming circular flux surfaces the resulting power density $\frac{\text{d}P}{\text{d}r}$ from integrating over the angle, θ, for both $r \ll L$ and $r \gg L$, is

$$\frac{\text{d}P}{\text{d}r} \propto_r \min\left(\sqrt{\pi}r, L\exp\left(-\frac{2r^2}{w^2}\right)\right). \tag{37}$$

The proportionality constant is set by the total absorbed power from equation (7).

4. Ionisation avalanche in Wendelstein 7-X

The above model is used to simulate the plasma start-up under conditions relevant to the Wendelstein 7-X (W7-X) stellarator. W7-X is equipped with superconducting coils that generate a magnetic field with an accuracy of one part in 100 000 [38]. Plasma breakdown is typically achieved via ECRH, using 140 GHz gyrotrons that launch Gaussian beams in X2-mode polarisation [39].

The model parameters are chosen to reflect the W7-X geometry and operating conditions. The radial size is set to $r_{\text{max}} = 0.51\,\text{m}$, the beam width $w = 4\,\text{cm}$, the diffusion coefficient L_{ii} is derived from D_{ii} following Beidler *et al* [35]. The power is set to $P = 2\,\text{MW}$.

The value of the coefficient $\bar{A}_0$ relevant for W7-X condition is around 650. It corresponds to $\frac{1}{B}\frac{\text{d}B}{\text{d}x} \sim 0.03\text{m}^{-1}$ (see figure 2). The major radius is set to $R = 5.52\,\text{m}$ and the magnetic field

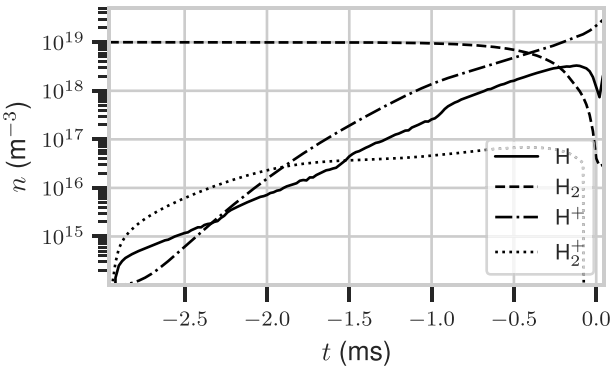

Figure 6. Density evolution at $r = 0$.

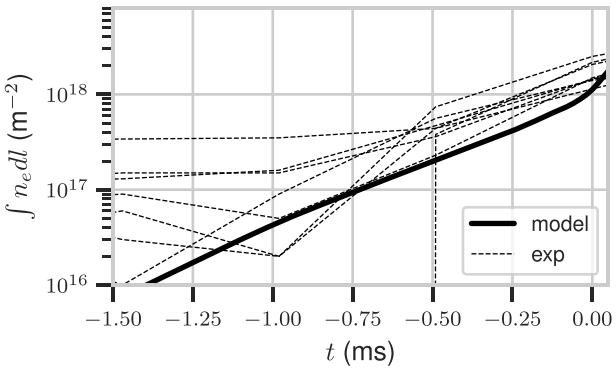

Figure 7. Line-integrated density from several W7-X experiments in dashed lines and from modelling in solid line.

strength is 2.5 T on axis. Perpendicular wave propagation is assumed. The absorption length-scale L is given by the resonance width in figure 4, that is $\Delta B_0/B = 0.77\,\mathrm{mTT}^{-1}$ (figure 4). For W7-X, $\frac{dB}{dz} \approx 0.97\,\mathrm{Tm}^{-1}$, and thus $L \approx 2\,\mathrm{mm}$.

The typical pre-fill hydrogen density is $n_{\mathrm{H}_2} = 1 \times 10^{19}\,\mathrm{m}^{-3}$. We begin our computation with an initial ion density of $n_{\mathrm{H}_2^+} = n_{\mathrm{H}^+} = 1 \times 10^{14}\,\mathrm{m}^{-3}$. The initial temperature is assumed to be room temperature of 300 K. The equations (equations (24) and (26)) are numerically integrated using the FiPy finite-volume solver [40].

The temporal evolution of the core densities for all species is presented in figure 6. Initially, $n_{\mathrm{H}_2^+}$ is the dominant ion species. As the dissociation rate of $n_{\mathrm{H}_2^+}$ increases, the density of n_{H^+} eventually surpasses that of $n_{\mathrm{H}_2^+}$, thereby becoming the dominant ion species. The atomic hydrogen density n_{H} exceeds the molecular hydrogen density n_{H_2} towards the end of the avalanche process.

Figure 7 shows the line-integrated electron density predicted by the model alongside data from a selection of W7-X discharges (#20221129.36, #20221130.31, #20230117.40, #20230316.16, #20230315.20, #20230316.23, #20230316.51). These discharges have similar key parameters, including a total ECRH power of 2 MW, on-axis heating, and hydrogen pre-fill conditions, as inferred from the final electron density. The experimental values obtained from the interferometer diagnostic [41] are shown as dashed lines, while the model prediction is represented by the solid line. Time zero, $t = 0$, is defined as the moment when the line-integrated electron density reaches $\int n_e \mathrm{d}l = 1 \times 10^{18}\,\mathrm{m}^{-2}$. There is reasonable agreement between the model and the aggregated experimental data, except at very early times, when the measurements are inherently unreliable.

The ionisation avalanche is characterised by a distinct phase of nearly constant electron temperature, which is established after an initial rapid temperature rise. This behaviour is illustrated in figure 8, which shows the temporal evolution of the electron temperature at $r = 0$ for the above parameters. Initially, the heating exceeds the energy loss plus change in internal energy. However, a balance between heating, energy loss, and rise in internal energy establishes quickly. Even though this balance occurs at an electron temperature

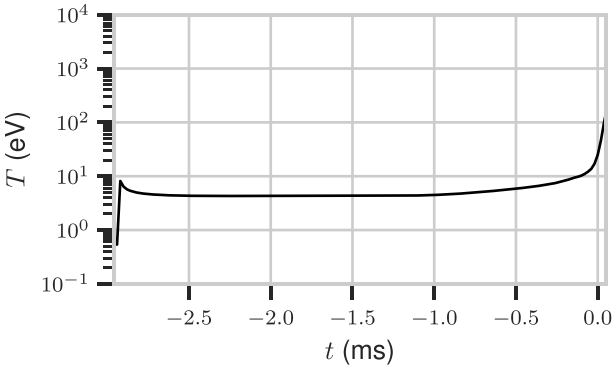

Figure 8. Temperature evolution at the core.

below 13.6 eV, the tail of the Maxwellian distribution suffices to drive the ionisation avalanche depicted in figure 6.

During the temperature plateau phase, the heating power approximately balances the rise in internal energy due to ionisation, and losses due to ionisation, charge exchange, and radiation. As the dominant losses, rise in internal energy as well as power absorption scale linearly with the electron density, the system naturally evolves towards a temperature plateau. Eventually, as the plasma approaches full ionisation, these loss processes diminish sharply, leading to an increase in temperature. At this stage, the model assumptions are no longer valid.

Notably, the temperature plateau phase emerges robustly across a wide range of power levels. The only exception occurs for a very high power such that the gas becomes ionised during the initial heating phase, thereby bypassing the plateau entirely.

The contributions to the change in electron temperature are shown in figure 9. The dominant term is the line radiation, primarily because the hydrogen density is much higher than that of any other species. The second dominant term is the heating and overcoming of the ionisation potential. Charge exchange is important for temperatures near one to two eV. At low T_e, the ionisation process can stagnate.

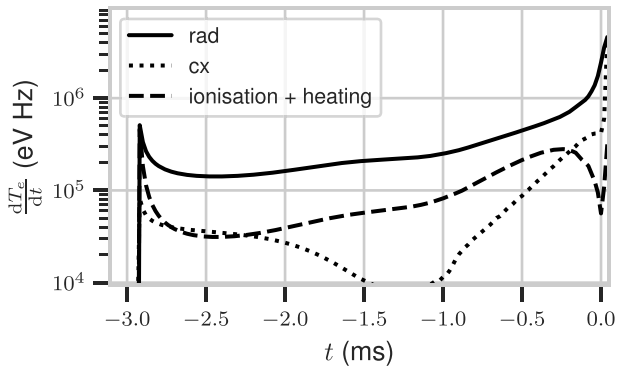

Figure 9. Evolution of the temperature loss terms.

5. Condition for sufficiently fast breakdown

A stagnation in electron density, n_e, indicates a failed breakdown scenario. One possible cause of such failure is insufficient plateau temperature. A critical electron temperature exists: for T_e exceeding this threshold, the decrease in neutral hydrogen density, H, leads to a reduction in power losses, allowing the electron temperature to rise. Conversely, if T_e remains below this critical value, the system settles into a true steady state characterised by partial ionisation.

Near the critical temperature, ionisation dynamics are particularly slow. For instance, achieving a 50/50 mixture of H and H^+ requires an electron temperature of approximately $T_e \approx 1.3\,\mathrm{eV}$. At this temperature, the ionisation rate coefficient of hydrogen is roughly 2000 times lower than in the W7-X breakdown scenario previously discussed, implying breakdown timescales on the order of tens of seconds.

Breakdown failure may also result from excessive radiative losses exceeding the available input power. To prevent this, the required input power for achieving $T_e = 4\,\mathrm{eV}$ is given by

$$P_0 \gtrsim 4.4 \times 10^{-39}\,\mathrm{MW\,m^3} \iiint n_{i,\mathrm{H_2}}^2\,\mathrm{d}V,$$

where $n_{i,\mathrm{H_2}}$ denotes the initial molecular hydrogen density. Here, the radiative loss term $(2n_{\mathrm{H_2}} + n_{\mathrm{H}})n_e$ has been replaced by its optimal estimate $n_{\mathrm{H_2}}$ for simplicity. Assuming a uniform distribution of electron density over one Gaussian beam width, yields

$$P_0 \gtrsim 0.9\,\mathrm{kW} \cdot n_{\mathrm{H_2}}^2 w^2 R_0,$$

where w is the beam width in centimetres, R_0 is the characteristic scale length in metres, and $n_{\mathrm{H_2}}$ is expressed in units of $1 \times 10^{19}\,\mathrm{m^{-3}}$. For typical machine parameters such as those of W7-X or TJ-II, this threshold is generally exceeded.

In W7-X, maximum allowable breakdown time is set by the stray radiation limits. In particular, this sets the power required for a breakdown. Theoretically, lower power than this threshold could achieve breakdown. However, because the reaction rate coefficient decreases sharply with electron core temperature, such a breakdown would require an unreasonably long time. Such discharges are therefore aborted. The breakdown time is therefore determining the breakdown condition in practice. It manifests as a sufficiently high plateau temperature equation (26) so that the ionisation process is sufficiently fast to avoid excessive stray radiation. Below, we derive an estimate for the plateau temperature.

In an optimised configuration, the diffusion term can be neglected. The steady state of equation (26) is given by

$$\hat{S} - \hat{L} = 0. \tag{38}$$

In the case of weak absorption, this equation becomes

$$P_0 \frac{\langle n_e \rangle_y}{n_e} \frac{\bar{A}_0 m 2 N_\perp^2 \eta}{\pi^2 R_0 B^2 w^2} \min\left(1, \frac{L}{\sqrt{\pi} r} \exp\left(-\frac{2r^2}{w^2}\right)\right) = \frac{\bar{d}}{2\langle |v_x| \rangle} \hat{L}. \tag{39}$$

This equation is written so that the left-hand side depends on both $n_e(r,t)$, and r, while the right-hand side depends on $T_e(r)$. The weak dependence of n_e on the right-hand side via the reaction rates is ignored. To determine the plateau temperature, $\frac{\langle n_e \rangle_y}{n_e}$ must be calculated, which in principle requires the exact time evolution.

However, since the gradient of T_e must be 0 at the core, the right-hand side must be approximately independent of r, implying the same for the left-hand side. Therefore, we assume the following form for the electron density profile:

$$n_e \approx n_{e0} \min\left(1, \frac{L}{r\sqrt{\pi}} \exp\left(-\frac{2r^2}{w^2}\right)\right), \tag{40}$$

where n_{e0} is the core density.

The density profile is shown in figure 10. The analytically predicted density profile in equation (40) is shown with the dashed line, and the solid line displays a snapshot of the profile from the numerical solution presented in figures 8 and 9. Despite the predicted profile not taking the density evolution equation into account, the two profiles agree.

The y-averaging in the power deposition term can then be performed analytically, yielding

$$\begin{aligned} \langle n_e \rangle_y &= \frac{\int_{-\infty}^{\infty} n_{e0} \min\left(1, \frac{L}{y\sqrt{\pi}} \exp\left(-\frac{2y^2}{w^2}\right)\right) \exp\left(-\frac{2y^2}{w^2}\right) \mathrm{d}y}{\int_{-\infty}^{\infty} \exp\left(-\frac{2y^2}{w^2}\right) \mathrm{d}y} \\ &\approx n_{e0} \frac{\sqrt{2}L}{\pi w} \left(2 - \mathrm{Ei}\left(-\frac{4L^2}{\pi w^2}\right)\right) \end{aligned} \tag{41}$$

where Ei is the exponential integral. The quasi steady-state core temperature is thus given by the solution to

$$P_0 \frac{\sqrt{2}L}{\pi w} \left(2 - \mathrm{Ei}\left(-\frac{4L^2}{\pi w^2}\right)\right) \frac{\bar{A}_0 m 2 N_\perp^2 \eta}{\pi^2 R_0 B^2 w^2} = \frac{\bar{d}}{2\langle |v_x| \rangle} \hat{L}. \tag{42}$$

This dependence of the plateau temperature is shown in figure 11, where the plasma is assumed to contain only $n_{\mathrm{H_2}}$

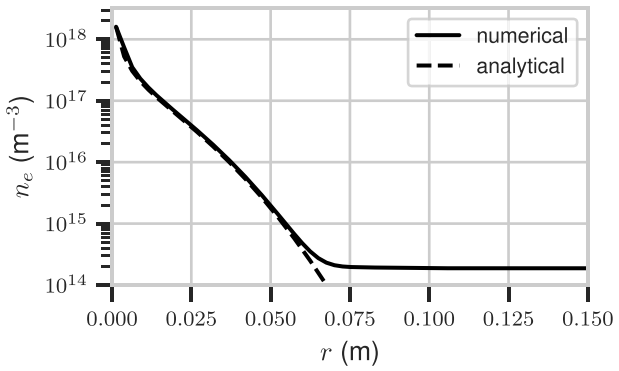

Figure 10. Predicted electron density profile from equation (40) in dashed. Electron density profile at −0.96 ms of model showed in figures 6 and 7 with black line. Initial electron density was $2 \times 10^{14}\,\mathrm{m}^{-3}$.

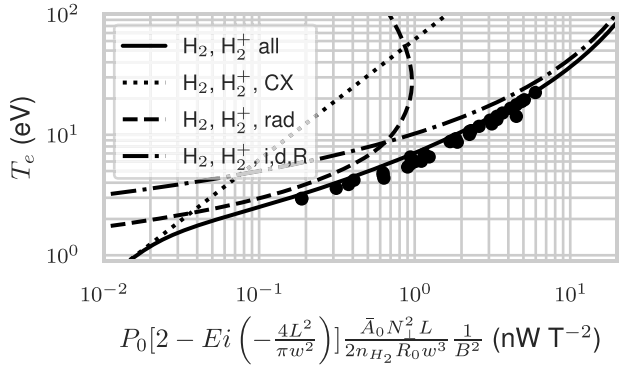

Figure 11. Plateau temperature from equation (42) as function of machine parameters in solid line. Achieved plateau temperature through different simulations are shown with dots for initial H_2 gas. The power loss given by the solid line has different contributions. These are charge exchange, given by the dotted line, radiation, given by the dashed line and ionisation, recombination and disassociation, given by the dash-dotted line. The sum of all three for fixed temperature yields the solid line. These contribution depend on the exact mixture of constituents, and are here given by $n_{H_2} = 5 \times 10^{18}\,\mathrm{m}^{-3}$ and $n_{H_2^+} = 1 \times 10^{14}\,\mathrm{m}^{-3}$. Although the power loss is dependent on exact densities, the variation of the solid line is slight in the limit of non-equilibrium high neutral density.

and $n_{H_2^+}$. The r.h.s. scales linearly with the former and is independent of the latter, whereas the l.h.s. is independent of both. Simulated plateau temperatures from full time-dependent solutions are shown with circles.

Despite knowing the radial density profile and plateau temperature, a numerical solution is necessary to determine the ionisation avalanche time. We will compare several of such numerical solutions with the breakdown times presented in figure 10*(a)* and 10*(b)* by Cappa *et al* [14], which were obtained experimentally. This time is defined as the first H_α peak. These discharges were performed in TJ-II.

TJ-II has the following parameters $R = 1.5\,\mathrm{m}$, $B = 0.95\,\mathrm{T}$ and $w = \sqrt{\frac{1}{2}}\sqrt{(4\,\mathrm{cm})^2 + (2.4\,\mathrm{cm})^2} \approx 3.3\,\mathrm{cm}$ [42, 43], where the beam width differs in different directions and the root mean squared value was taken. For the coefficient $\bar{A}_0$, and L, the different B-field derivatives are summarised in table 1. The

Table 1. The different B derivatives for the different $N_\parallel$ cases and their respective $\bar{A}$ and resonance length scales L.

$N_\parallel$	$\frac{\mathrm{d}\ln B}{\mathrm{d}x}$ (m^{-1})	$\frac{\mathrm{d}B}{\mathrm{d}k}$ ($\mathrm{T\,m}^{-1}$)	$\bar{A}$	L (mm)
0	0.06	1.03	124	1.3
0.3	0.11	1.07	65	2.2
0.57	0.23	1.00	33	4.6

values of $\bar{A}$ and L are calculated using the scaling compared to the reference value in figures 2 and 4.

The initial experimental pressure was $P \approx 5 \times 10^{-5}$mbar [14], which translates to $n_{H_2} = 1.2 \times 10^{18}\,\mathrm{m}^{-3}$. Determining the initial electron density is challenging. However, the breakdown time only depends on it logarithmically. We take the initial density to be $1 \times 10^7\,\mathrm{m}^{-3}$, which corresponds to the density expected at an altitude of 60 km [44].

In this parameter regime, the ratio of the electron toroidal transit time to the electron-neutral collision time is slightly less than unity. This condition formally violates the assumption of a Maxwellian velocity distribution. Since some particles will not slow down between the interactions. However, this does not compromise the validity of the model significantly, since the distribution function f may be represented as a superposition of Maxwellian distributions:

$$f(v) = \int_0^\infty \beta\left(\frac{1}{T}\right) \exp\left(-\frac{mv^2}{2T}\right) \mathrm{d}\left(\frac{1}{T}\right),$$

where $\beta(1/T)$ is the inverse Laplace transform of $f(v)$, up to a normalisation factor. Under this decomposition, the temperature dependence of the averaged absorption amplitude $\bar{A}$ is captured through integration over the weighting function $\beta(1/T)$. However, since this dependence is relatively week (see figure 5), we neglect it when taking the integral. Additionally, the width parameter d, which characterises the absorption profile, was found to be nearly independent of temperature.

The breakdown times dependency of a transmitted ECRH power and $N_\parallel$ is shown in figure 12. The square markers represent $N_\parallel = 0$, the circles represent $N_\parallel = 0.3$, and the triangles represent $N_\parallel = 0.57$. Although the value of $N_\parallel$ determines the label, the beam path differs for each $N_\parallel$. This results in a change to the magnetic field derivative, see table 1. The breakdown time obtained by numerical solution is shown with black markers, whereas the experimental data from Cappa *et al* [14] is shown with grey markers. The vacuum polarisation of the ECRH beam is such that the power couples only with E^2 to within 0.5 %. The transmitted power in the experiments is calculated from the gyrotron power via an approximate transmission efficacy of 90 % [42].

The experimental breakdown time is defined as the time from the gyrotron turn-on to the first H_α emission peak. The model breakdown time is defined similarly, however the volume integrated H_α emission is considered. Good quantitative agreement is found. The power required for a specific breakdown time is in the correct order of magnitude, differing by no more than a factor of 1.8.

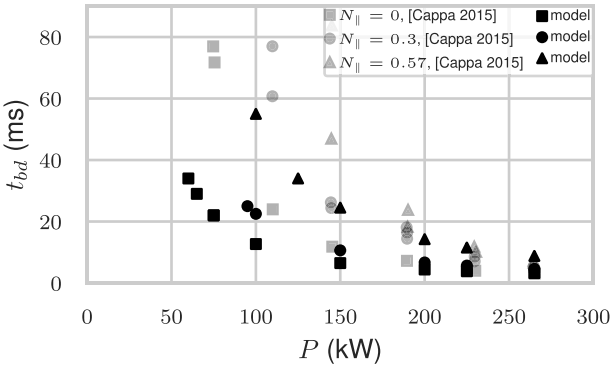

Figure 12. Breakdown time versus transmitted ECRH power for different $N_\parallel$. Numerical solutions using the model in black markers, experimental data from Cappa *et al* [14] in grey markers. $N_\parallel \in \{0, 0.3, 0.57\}$ are shown with squares, circles and triangles respectively. Each $N_\parallel$ is associated with different B-field derivatives, which are reported in table 1.

The qualitative dependence is also captured: triangles are above circles, which are above squares, for both the experiments displayed with grey markers and the simulations displayed with black markers. Despite the $N_\parallel$ label, the actual change in breakdown time is caused by the different magnetic field derivative at the beam centre. The corresponding change in $\frac{\mathrm{d}\ln B}{\mathrm{d}x}$ for different $N_\parallel$ is found in table 1. This derivative change affects the efficacy of the electron wave coupling, as can be seen in the bottom row of figure 2.

Note that the relation between breakdown time and power can be roughly estimated by solving

$$\frac{\partial n_e}{\partial t} = n_e n_{\mathrm{H}_2} \left(R_{\mathrm{e}+\mathrm{H}_2 \mapsto \mathrm{H}_2^+ + 2\mathrm{e}} + R_{\mathrm{e}+\mathrm{H}_2 \mapsto \mathrm{H}^+ + \mathrm{H} + 2\mathrm{e}} \right), \tag{43}$$

with solution

$$t_{\mathrm{bd}} \approx \frac{\log\left(\frac{2n_{\mathrm{H}_2}}{n_{e0}}\right)}{n_{\mathrm{H}_2}\left(R_{\mathrm{e}+\mathrm{H}_2 \mapsto \mathrm{H}_2^+ + 2\mathrm{e}} + R_{\mathrm{e}+\mathrm{H}_2 \mapsto \mathrm{H}^+ + \mathrm{H} + 2\mathrm{e}} \right)} \tag{44}$$

where $n_{\mathrm{e}0}$ is the initial free electron density and the rates $R_{\mathrm{e}+\mathrm{H}_2 \mapsto \mathrm{H}_2^+ + 2\mathrm{e}}$, and $R_{\mathrm{e}+\mathrm{H}_2 \mapsto \mathrm{H}^+ + \mathrm{H} + 2\mathrm{e}}$ are evaluated at the plateau temperature equation (42). This estimate gives a maximum factor of 5.2 between experimental and estimated power needed for a specific breakdown time, i.e. 3 times worse than that of the simulation. As discussed previously, the practical breakdown condition is set by the acceptable experimental time for plasma formation, i.e. sufficiently large reaction rates R_* at the plateau temperature. For high temperatures, these reaction rates stagnate, thus explaining the weaker power dependence for high input powers in figure 12.

6. Conclusion

Although second-harmonic X-mode ECRH is routinely employed for plasma start-up in stellarators, a quantitative criterion for plasma breakdown has not yet been established. In this work, a model for ECRH power absorption in the low-density pre-fill phase is formulated and coupled to a simplified hydrogen ionisation framework to describe the onset of ionisation avalanche. A semi-analytical expression for the electron temperature during the avalanche phase is derived as a function of relevant machine parameters, providing an estimate for successful breakdown condition.

To this end, electron orbits crossing the beam are analysed. For the typical electron energy during ionisation avalanche, these orbits neither constitute of an adiabatic orbit, nor a small energy kick. Electrons can gain substantial energy without experience several non-linear energy excursions. The average power absorption of electrons is studied numerically. This is combined with the power loss during the ionisation avalanche.

It turns out that the electron temperature reaches a quasi-steady state during the ionisation avalanche due to a balance of power between losses from radiation, ionisation and charge exchange, and wave absorption—all of which scale approximately linearly with electron density. To achieve plasma formation, the quasi-steady-state temperature must be sufficiently high for the ionisation rate to overcome the recombination rate. Despite this formal condition for plasma breakdown, in practice, the breakdown condition is set by a sufficiently high ionisation rate such that the ionisation occurs before maximal allowable stray radiation occurs.

Despite knowing the quasi-steady state temperature and the electron density profile, the time taken to achieve breakdown needs to be obtained numerically. We compare this breakdown time with experimental data and find good qualitative agreement, despite the fact that the initial electron density is not known, since the breakdown time only logarithmically dependent on the initial condition.

Acknowledgments

The authors would like to thank Eric Hollmann for providing results of the calculations using the model in [34], which we used to benchmark our ionisation calculations.

This work has been carried out within the framework of the EUROfusion Consortium, funded by the European Union via the Euratom Research and Training Programme (Grant Agreement No. 101052200–EUROfusion). Views and opinions expressed are however those of the author(s) only and do not necessarily reflect those of the European Union or the European Commission. Neither the European Union nor the European Commission can be held responsible for them.

Appendix. Maxwell distribution assumption

An electron, accelerated by the wave, to some random speed V_0 undergo several collisions, after each obtaining a new speed V_i from a push Δv_i. The end speed $V_N = V_0 + \sum_{i=1}^{N} \Delta v_i$ is Maxwell distributed as $N \to \infty$ if Δv_i are independent. The velocity change Δv_i is however dependent on V_{i-1} through the double collisional cross sections. However, the sequence is an adapted process and according to the Doob decomposition theorem Δv_i can be decomposed into a sum of a Martingale and a predictable process (an predictable process is adapted

and can be decomposed once again). The central limit theorem also holds for Martingales (under some conditions for the variance). It is not unreasonable to expect (after sufficiently many collisions), although not proved, that an electron, regardless of collisional form, attains a Maxwell distribution. A clear counter example of random interactions not attaining the Maxwell distribution is the quasi-linear wave–particle interaction, but there the wave contains non-thermal free energy (whereas the neutrals do not).

A.1. Small discussion of other harmonics

For other harmonics, the Hamiltonian does attain the same form as equation (2), albeit the factor before $\cos(\chi)$ changes (see for example [22]). Nevertheless, if the energy change scales with E^2, a similar analysis can be made to extract some information of $\Delta\gamma$. One must then calculate $\bar{A}_*$ for some wave-mode * (X1, O1, X3, etc) to find the effectiveness of the wave-mode. As an example, some typical value of $\bar{A}_{X3}$ for W7-X relevant parameters are several orders of magnitude lower than for X2, implying that several orders of magnitude more power is most likely necessary to achieve start up with pure X3. At such powers, it is questionable if the assumptions made to obtain equation (2) are still valid.

ORCID iDs

C. Albert Johansson 0000-0002-0956-9186
Pavel Aleynikov 0009-0002-3037-3679
Alvaro Cappa 0000-0002-2250-9209

References

[1] Townsend J.S. 1915 Electricity in gases *J. Rntgen Soc.* **11** 87–87
[2] Mueller D. 2013 The physics of tokamak start-up *Phys. Plasmas* **20** 058101
[3] Paschen F. 1889 Ueber die zum funkenübergang in luft, wasserstoff und kohlensäure bei verschiedenen drucken erforderliche potentialdifferenz *Ann. Phys., Lpz.* **273** 69–96
[4] Lloyd B., Carolan P.G. and Warrick C.D. 1996 ECRH-assisted start-up in ITER *Plasma Phys. Control. Fusion* **38** 1627–43
[5] Lloyd B., Jackson G.L., Taylor T.S., Lazarus E.A., Luce T.C. and Prater R. 1991 Low voltage ohmic and electron cyclotron heating assisted startup in DIII-D *Nucl. Fusion* **31** 2031
[6] Jackson G.L., deGrassie J.S., Moeller C.P. and Prater R. 2007 Second harmonic electron cyclotron pre-ionization in the DIII-D tokamak *Nucl. Fusion* **47** 257
[7] Bucalossi J., Hertout P., Lennholm M., Saint-Laurent F., Bouquey F., Darbos C., Traisnel E. and Trier E. 2008 First experiments of plasma start-up assisted by ECRH on Tore Supra *Nucl. Fusion* **48** 054005
[8] Stober J., Jackson G.L., Ascasibar E., Bae Y.-S., Bucalossi J., Cappa A., Casper T., Cho M.-H., Gribov Y., Granucci G., Hanada K. 2011 ECRH-assisted plasma start-up with toroidally inclined launch: multi-machine comparison and perspectives for ITER *Nucl. Fusion* **51** 083031
[9] Granucci G. *et al* (FTU Team) 2015 Experiments and modeling on FTU tokamak for EC assisted plasma start-up studies in ITER-like configuration *Nucl. Fusion* **55** 093025
[10] Bae Y.S. *et al* (the KSTAR Team) 2008 ECH pre-ionization and assisted startup in the fully superconducting KSTAR tokamak using second harmonic *Nucl. Fusion* **49** 022001
[11] Kajiwara K., Ikeda Y., Seki M., Moriyama S., Oikawa T. and Fujii T. (JT-60 Team) 2005 Electron cyclotron heating assisted startup in JT-60 U *Nucl. Fusion* **45** 694
[12] Cappa A. and Castejón F. 2004 Electron energy distribution function during second harmonic ECRH plasma breakdown *Nucl. Fusion* **44** 406
[13] Carter M.D., Callen J.D., Batchelor D.B. and Goldfinger R.C. 1986 Collisional effects on coherent nonlinear wave-particle interactions at cyclotron harmonics *Phys. Fluids* **29** 100–9
[14] Cappa A.., Ascasíbar E., Castejón F., Tafalla D., Tabarés F., Ochando M., Romero J., de la Cal E., Martínez J. and Nagasaki K. 2015 Second harmonic ECRH breakdown experiments in the TJ-II stellarator *Nucl. Fusion* **55** 043018
[15] Seol J., Hegna C.C. and Callen J.D. 2009 Nonlinear cyclotron harmonic absorption *Phys. Plasmas* **16** 052512
[16] Johansson C.A. and Aleynikov P. 2024 Electron cyclotron resonance during plasma initiation *J. Plasma Phys.* **90** 905900103
[17] Jaeger F., Lichtenberg A.J. and Lieberman M.A. 1972 Theory of electron cyclotron resonance heating. i. Short time and adiabatic effects *Plasma Phys.* **14** 1073–100
[18] Zvonkov A.V. and Timofeev A.V. 1986 Relativistic effects in the formation of braided electrons during cyclotron heating *Sov. J. Plasma Phys. (Engl. Transl.)* **12** 238–40
[19] Nevins W.M., Rognlien T.D. and Cohen B.I. 1987 Nonlinear absorption of intense microwave pulses *Phys. Rev. Lett.* **59** 60–63
[20] Neishtadt A.I. and Timofeev A.V. 1987 Autoresonance in electron cyclotron heating of a plasma *Zh. Eksp. Teor. Fiz* **93** 1706–13
[21] Suvorov E.V. and Tokman M.D. 1988 Generation of accelerated electrons during cyclotron heating of plasmas *Sov. J. Plasma Phys.(Engl. Transl.)* **14** 8
[22] Farina D. and Pozzoli R. 1991 Nonlinear electron-cyclotron power absorption *Phys. Fluids B* **3** 1570–5
[23] Kotel'Nikov I.A. and Stupakov G.V. 1991 Adiabatic theory of nonlinear electron-cyclotron resonance heating *J. Plasma Phys.* **45** 19–27
[24] Kennel C.F. and Engelmann F. 1966 Velocity space diffusion from weak plasma turbulence in a magnetic field *Phys. Fluids* **9** 2377–88
[25] Kaufman A.N. 1972 Quasilinear diffusion of an axisymmetric toroidal plasma *Phys. Fluids* **15** 1063–9
[26] Timofeev A.V. and Tokman M.D. 1994 Quasi-linear equation for electron cyclotron resonance interaction with monochromatic radiation in magnetic traps *Plasma Phys. Rep.* **20**
[27] Shalashov A.G., Gospodchikov E.D. and Izotov I.V. 2020 Electron-cyclotron heating and kinetic instabilities of a mirror-confined plasma: the quasilinear theory revised *Plasma Phys. Control. Fusion* **62** 065005
[28] Farina D. 2018 Nonlinear collisionless electron cyclotron interaction in the pre-ionisation stage *Nucl. Fusion* **58** 066012
[29] Petviashvili V.I., Yan'kov V.V. and Timofeev A.V. 1989 *Reviews of Plasma Physics* vol 14 (Consultants Bureau)
[30] Kamendje R., Kasilov S.V., Kernbichler W. and Heyn M.F. 2003 Kinetic modeling of nonlinear electron cyclotron resonance heating *Phys. Plasmas* **10** 75–97
[31] Johansson C.A., Aleynikov P., Helander P. and Moseev D. 2025 Generation of energetic electrons during X2 ECRH start up *Nucl. Fusion* **65** 056009

[32] Reiter D., Baelmans M. and Börner P. 2005 The EIRENE and B2-EIRENE codes *Fusion Sci. Technol.* **47** 172–86
[33] Summers H 2004 ADAS manual 2.6 (available at: http://www.adas.ac.uk/manual.php)
[34] Hollmann E.M. *et al* 2019 Study of argon assimilation into the post-disruption runaway electron plateau in DIII-D and comparison with a 1D diffusion model *Nucl. Fusion* **59** 106014
[35] Beidler C.D. *et al* 2011 Benchmarking of the mono-energetic transport coefficients-results from the International Collaboration on Neoclassical Transport in Stellarators (ICNTS) *Nucl. Fusion* **51** 076001
[36] Sharda P., Krumholz M.R. and Federrath C. 2019 The role of the H2 adiabatic index in the formation of the first stars *Mon. Not. R. Astron. Soc.* **490** 513–26
[37] Janev R.K. *et al* 2012 *Elementary Processes in Hydrogen-Helium Plasmas: Cross Sections and Reaction Rate Coefficients* (Springer)
[38] Pedersen T.S. *et al* 2016 Confirmation of the topology of the Wendelstein 7-X magnetic field to better than 1:100,000 *Nat. Commun.* **7** 13493
[39] Laqua H.P. *et al* 2021 (the W7-X Team) High-performance ECRH at W7-X: experience and perspectives *Nucl. Fusion* **61** 106005 ust 2021
[40] Guyer J.E., Wheeler D. and Warren J.A. 2009 FiPy: partial differential equations with python *Comput. Sci. Eng.* **11** 6–15
[41] Brunner K.J., Akiyama T., Hirsch M., Knauer J., Kornejew P., Kursinski B., Laqua H., Meineke J., Trimiño Mora H. and Wolf R.C. 2018 Real-time dispersion interferometry for density feedback in fusion devices *J. Instrum.* **13** 09002
[42] Alejaldre C. *et al* 1999 First plasmas in the TJ-II flexible heliac *Plasma Phys. Control. Fusion* **41** A539
[43] Martínez-Fernández J. *et al* 2020 High power characterisation of the ECRH transmission lines and power deposition calculations in the TJ-II stellarator *Fusion Eng. Des.* **161** 112065
[44] Pfaff R.F. 2012 The near-earth plasma environment *Space Sci. Rev.* **168** 23–112